Journal of Biomedical Optics

SPIEDigitalLibrary.org/jbo

Video-rate fluorescence lifetime imaging camera with CMOS single-photon avalanche diode arrays and high-speed imaging algorithm

David D.-U. Li
Jochen Arlt
David Tyndall
Richard Walker
Justin Richardson
David Stoppa
Edoardo Charbon
Robert K. Henderson

Video-rate fluorescence lifetime imaging camera with CMOS single-photon avalanche diode arrays and high-speed imaging algorithm

David D.-U. Li,[a,b] Jochen Arlt,[c] David Tyndall,[b] Richard Walker,[b] Justin Richardson,[b,d] David Stoppa,[e] Edoardo Charbon,[f] and Robert K. Henderson[b]

[a]University of Sussex, Biomedical Engineering Group, Department of Engineering and Design, School of Engineering and Informatics, Brighton BN1 9QT, United Kingdom
[b]University of Edinburgh, Institute for Integrated Micro and Nano Systems, Joint Research Institute for Signal & Image Processing/Integrated Systems/Energy/Civil and Environmental Engineering, School of Engineering, Faraday Building, King's Buildings, Edinburgh EH9 3JL, Scotland, United Kingdom
[c]University of Edinburgh, SUPA, COSMIC, School of Physics and Astronomy, Joseph Black Building, King's Buildings, Edinburgh EH9 3JZ, Scotland, United Kingdom
[d]STMicroelectronics, 33 Pinkhill, Edinburgh EH12 7BF, Scotland, United Kingdom
[e]Fondazione Bruno Kessler, Smart Optical Sensors and Interfaces, 38122 Trento, Italy
[f]Delft University of Technology, Faculty Electrical Engineering, Mathematics and Computer Science, Mekelweg 4, 2628CD Delft, The Netherlands

Abstract. A high-speed and hardware-only algorithm using a center of mass method has been proposed for single-detector fluorescence lifetime sensing applications. This algorithm is now implemented on a field programmable gate array to provide fast lifetime estimates from a 32 × 32 low dark count 0.13 μm complementary metal-oxide-semiconductor single-photon avalanche diode (SPAD) plus time-to-digital converter array. A simple look-up table is included to enhance the lifetime resolvability range and photon economics, making it comparable to the commonly used least-square method and maximum-likelihood estimation based software. To demonstrate its performance, a widefield microscope was adapted to accommodate the SPAD array and image different test samples. Fluorescence lifetime imaging microscopy on fluorescent beads in Rhodamine 6G at a frame rate of 50 fps is also shown. [DOI: 10.1117/1.3625288]

Keywords: fluorescence lifetime imaging microscopy; time-resolved imaging; photon counting; complementary metal-oxide-semiconductor; single-photon avalanche diode; center-of-mass.

Paper 11197RR received Apr. 19, 2011; revised manuscript received Jul. 20, 2011; accepted for publication Jul. 21, 2011; published online Sep. 15, 2011.

1 Introduction

A single-photon avalanche diode (SPAD), when biased at above its breakdown voltage, can be triggered by a photon that results in a self-sustaining avalanche multiplication process.[1] Its gain is so large that its output current can be easily converted into a digital signal without using complex front-end amplifiers deteriorating the signal-to-noise (SNR) ratio.[2] With such single-photon sensitivity, SPADs are suitable for photon-starved applications such as single molecule detection.[3,4] Thanks to the progress of semiconductor technology, SPAD arrays have been fabricated in a low-cost complementary metal-oxide-semiconductor (CMOS) process for three dimensional ranging and fluorescence lifetime sensing applications.[5–8] The doubt about higher dark count caused by exacerbated tunneling effect on an advanced CMOS process has been dispelled by the latest developments in deep sub-micron SPAD structures.[9–12] A dark count rate (DCR) of 25 Hz has been successfully reported in standard 0.13 μm CMOS process,[10] and low dark-count prototypes moving to 90 nm CMOS process node to miniaturize the pixel size or to enhance the quantum efficiency in the near-infrared spectral range have also been recently published.[11,12] Much larger SPAD arrays can be expected to facilitate fluorescence lifetime imaging microscopy (FLIM) applications.

Packing SPADs in arrays provides more flexibility as SPADs can work independently or in a group in combination with a multi-beam confocal imaging microscope.[13] The SPAD array can provide a platform for both wide-field and confocal scanning microscopy.

In the past, fluorescence lifetime imaging with high spatial resolution has been achieved by applying confocal scanning microscopes. The fluorescence histogram was recorded by a high-resolution time-to-digital converter (TDC) in a time-correlated single-photon counting (TCSPC) module. The data was stored in memory and then post-processed using maximum-likelihood-estimation (MLE) or least-square method (LSM)-based curve-fitting software pixel-by-pixel to generate a lifetime image. Although the MLE (or LSM) has merits of wide resolvability range and high photon efficiency, and usually hundreds of photons are enough to reach an acceptable accuracy,[14,15] the data acquisition is still slow (measurement time $= N_x \times N_y/f_p$, where f_p is the scanning frequency and $N_x \times N_y$ is the dimension of the array) and limits the systems to imaging only stationary objects. In many biological applications, real-time FLIM imaging for monitoring cell dynamics in low light level is desirable.

Address all correspondence to: David Li, University of Sussex, Department of Engineering and Design, School of Engineering and Informatics, Biomedical Engineering Group, Richmond Building, Brighton, BN1 9QT United Kingdom. Tel: +44 (0)1273873513; E-mail: david.li@sussex.ac.uk.

1083-3668/2011/16(9)/096012/12/$25.00 © 2011 SPIE

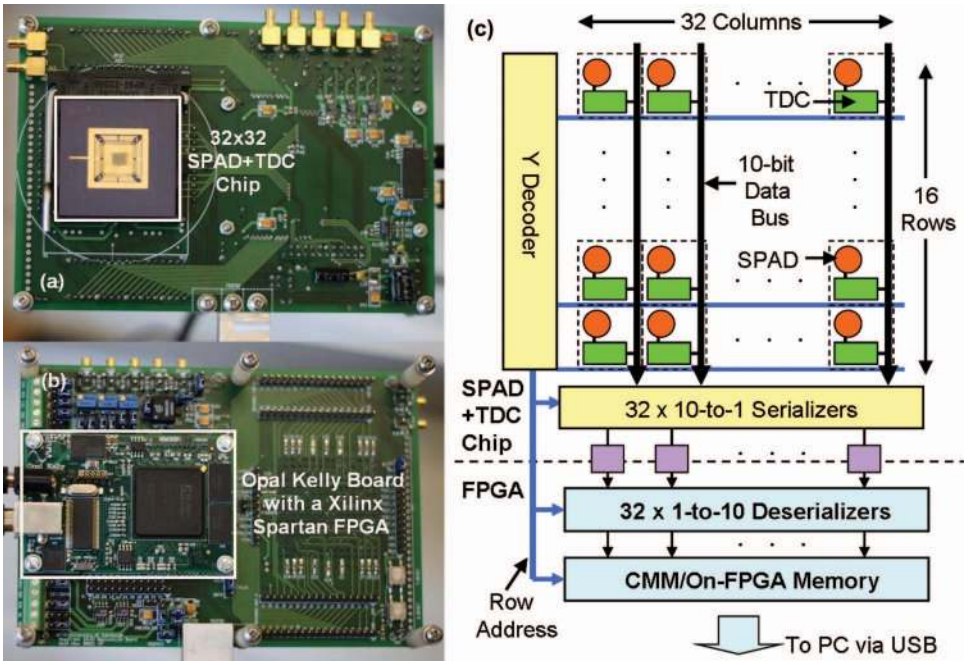

Fig. 1 (a) Top view, (b) bottom view of imager assembly with a 32×32 CMOS SPAD + TDC chip and an Opal Kelly board containing a Xilinx Spartan-III FPGA, and (c) 32×16 SPAD + TDC array and FPGA implementation of CMM.

There are real-time time-domain and frequency-domain FLIM systems available for wide-field applications. The time-domain FLIM systems usually employ time-gated detection.[16] Gated intensified charge-coupled device (CCD) cameras with a tunable delay from the excitation pulse and a given gate width are typically used to construct the fluorescence decay. Usually, a series of intensity images at different delays are acquired to generate a lifetime image, and attempts to solve double-exponential decays with multiple gates have also been reported.[17] For wide-field frequency domain FLIMs, they are typically implemented using optical image intensifiers.[18,19] Directly modulating the gain of a CCD camera has also been implemented.[20] Most of the systems mentioned above are CCD-based with multiple-channel plate intensifiers and usually require high voltage supplies (tens to hundreds of volts) or cooling systems. The quantum efficiency, DCR, physical size, spectral detection range, and required driving voltage for the latest reported SPADs, on the other hand, have been greatly improved during the past two years[6–12] This enables rapid advances in the development of high-speed FLIM cameras. With such SPAD-based systems we aim to provide: 1. fast lifetime previews, 2. intensity/lifetime imaging, 3. raw arrival time for detailed analysis, 4. a platform for both wide-field and confocal scanning microscopy, 5. compact, low voltage, and low cost solutions, and 6. flexibility to configure the cameras for other applications, such as fluorescence correlation spectroscopy (FCS) or Förster resonance energy transfer.

We have proposed a high-speed digital FLIM algorithm for a lifetime sensing system based on the center of mass method (CMM), and demonstrated its feasibility on real data collected by a single 0.35 μm CMOS SPAD and a single photon multiplier tube system.[14] It was proven to be suitable for sensing and confocal scanning applications. To apply the CMM for imaging applications, we need to collect arrival time information of every detected photon event for each pixel. This can be achieved by integrating TDCs in-pixel. Richardson et al. reported a low power 10-bit TDC array (with fast and slow TDC test sub-arrays)[21] with integrated low dark count SPADs (Ref. 10) to create a single chip TCSPC sensor in a 0.13 μm standard CMOS imaging process. The chip operates at a frame rate of 1 MHz and contains global calibration circuitry to maintain uniformity, and a time resolution of 54 ps has been achieved. The quantum efficiency of the SPAD is 28% at a wavelength of 500 nm with 80% of the pixels below a DCR of 50 Hz at room temperature. The imager can operate in a time-correlated mode for lifetime imaging or in a time-uncorrelated mode for intensity imaging. It can also be configured for confocal scanning and FCS applications[13] such that multiple SPAD pixels can be grouped together and greatly improve the photon collecting speed. The in-pixel TDCs can generate raw arrival time data, which can be sent to a PC and post-processed by curve fitting software. To increase the imaging speed, the raw arrival time data can be processed by on-field programmable gate array (FPGA) CMM processors. With CMM, video-rate FLIM imaging for biological applications can be achieved. Figures 1(a)–1(c) show the imager assembly including a 32×32 SPAD plus TDC chip and an Opal Kelly board containing a Xilinx Spartan-III FPGA,[22] on which the CMM is implemented.

The full range of TDCs should be able to accommodate commonly used samples with fluorescence lifetime, ranging from sub-nanosecond to tens of nanoseconds. Applying previously proposed CMM (Ref. 14) on a 10-bit TDC array with 54 or 78 ps resolution (TDC full range = 55 or 80 ns) will limit the lifetime resolvability range to less than 8 or 11 ns ($\tau < T/7$). To alleviate this problem, we can either apply TDCs with tunable resolution or simply employ a look-up table on-FPGA or with software without adding extra cost. The motivation of our paper is to develop low-cost hardware algorithms that can not only generate fast previews of the lifetime data but also remove I/O bottlenecks by compressing the raw timing data. For

simplicity and for a low cost solution, we assume the fluorescence emission is a single-exponential decay. The single-exponential decay model, however, is still useful to contrast different types of fluorophores. For diagnostic applications, obtaining lifetime contrast is probably more important than calculating the absolute values of lifetimes.[16] End-users can use the proposed algorithms to generate high-speed wide-field previews of lifetime data and switch to record raw data in wide-field or confocal scanning systems to produce high-resolution imaging on the area-of-interest. High-speed preview images are particularly useful for recording flow or protein-protein dynamics in live cells with minimum hardware/software resources.

In this paper, we first introduce a simple lifetime correction method that can be either implemented on firmware or software to enhance the lifetime resolvability range of the proposed CMM algorithm. The error equations for the corrected CMM algorithm will be given in Sec. 2. The correction allows the application of a higher laser repetition rate and therefore decreases the acquisition time. The FPGA implementation for the proposed algorithm on a low noise 32×32 0.13 μm CMOS SPAD plus TDC array will be introduced in Sec. 2. Image analysis of the SPAD array and video-rate FLIM will be presented in Sec. 3.

2 Material and Methods

2.1 *Fluorescence Lifetime Imaging Microscopy Algorithm Using Center-of-Mass Method*

For a fluorescence histogram with a single-exponential decay $f(t) = A\exp(-t/\tau)$ in a measurement window $0 \le t \le T$ recorded by the in-pixel 10-bit TDC,[21] its center of mass (CM) is approximated to the lifetime τ

$$\mathrm{CM} = \frac{\int_0^T t f(t)dt}{\int_0^T f(t)dt} = \tau - \frac{T\mathrm{e}^{-T/\tau}}{1-\mathrm{e}^{-T/\tau}}$$

$$\cong \tau_{\mathrm{CMM}} = \left(\frac{\sum_{j=0}^{M-1} jN_j}{N_c} + \frac{1}{2}\right)h, \quad (1)$$

where the TDC quantizes the measurement window into M time bins with the bin width of h. N_j is the number of recorded counts in the jth time bin ($j = 0, 1, \ldots, M-1$), and N_c is the total signal count within the measurement window. The accuracy and precision equations for CMM are given in Ref. 14, and rewritten as

$$\frac{\Delta\tau_{CMM}}{\tau} = \frac{h}{\tau}G(x) - 1, \quad (2)$$

$$\frac{\sigma\tau_{CMM}}{\tau} = \frac{h}{\tau\sqrt{N_c}}\frac{\sqrt{P(x)}}{(1-x)(1-x^M)}, \quad (3)$$

$$G(x) = \frac{1+x}{2(1-x)} - \frac{Mx^M}{1-x^M}, \quad (4)$$

$$P(x) = x - M^2x^M + (2M^2-2)x^{M+1} - M^2x^{M+2} + x^{2M+1}, \quad (5)$$

where $x = \exp(-h/\tau)$. Equation (1) can be easily implemented with a simple adder that can greatly reduce the readout bandwidth. The inverse precision and accuracy curves (easily transferred to dB) for the CMM and the 2-gate rapid lifetime determination (RLD) method[23–26] for a measurement window of $Mh = 2w_g = 1024h$ (w_g being the RLD gate width) and $N_c = 2^{17}$ are already shown in Ref. 14. From Eq. (1), the lifetime resolvability range of CMM for an error less than 0.5% is from $Mh/\tau = 7.5$ to 230, whereas that of RLD is from $Mh/\tau = 2.7$ to 7.7. Although the photon count required to reach the same accuracy is less than for CMM, it can be argued that using RLD can employ a higher laser repetition rate to achieve a faster acquisition speed. On the other hand, when the raw decay data is also required for detailed confocal scanning analysis using commercial iterative-based LSM software, it is desirable that a measurement window of 2 to 4τ is employed, which is clearly not favorable for CMM. A simple measure is needed to solve this problem.

2.2 *Enhancing Resolvability Range of Center of Mass Method*

The calculated lifetime τ_{CMM} only approximates to the exact one τ as a measurement window $T > 7\tau$. For $T < 7\tau$, Eq. (1) becomes a biased estimator, and it quickly converges to a less uncertain but wrong estimation smaller than the actual lifetime. To enhance the lifetime resolvability range, Eq. (1) needs to be re-examined. When $T < 7\tau$ is employed, the term $T\exp(-T/\tau)/[1 - \exp(-T/\tau)]$ in Eq. (1) cannot be neglected, and Eq. (1) is rewritten as

$$\frac{\tau_{\mathrm{CMM}}}{T} = \frac{\tau}{T} - \frac{\mathrm{e}^{-T/\tau}}{1-\mathrm{e}^{-T/\tau}}. \quad (6)$$

There is no closed form solution for Eq. (6), but it can be solved using the recursive approximation method as follows:

$$\frac{\tau_{i+1}}{T} = \frac{\tau_{\mathrm{CMM}}}{T} + \frac{\mathrm{e}^{-T/\tau_i}}{1-\mathrm{e}^{-T/\tau_i}}, \quad (7)$$

where $i = 0, 1, 2, \ldots, \tau_0 = \tau_{\mathrm{CMM}}$, and the process stops when an accuracy criteria is met $|\tau_{i+1} - \tau_i| < \varepsilon$. The root-finding process in Eq. (7), however, slowly converges as τ_{CMM}/T approaches 0.5. To increase the imaging speed, the recursive approximation results can be pre-stored in a look-up table (LUT) in software or in a vector using Matlab to directly map τ_{CMM} to τ. The resolution of the LUT can be further enhanced by introducing interpolation techniques. From Eqs. (1), (2), and (4), the accuracy for the new corrected lifetime becomes

$$\frac{\Delta\tau_{CMM,Corr}}{\tau} = \frac{h}{\tau}G(x) - 1 + \frac{T\mathrm{e}^{-T/\tau}}{\tau(1-\mathrm{e}^{-T/\tau})}$$

$$= \frac{h}{\tau}G(x) - 1 + \frac{h}{\tau}\frac{M\mathrm{e}^{-Mh/\tau}}{1-\mathrm{e}^{-Mh/\tau}} = \frac{h}{\tau}\frac{1+x}{2(1-x)} - 1, \quad (8)$$

where $x = \exp(-h/\tau)$ and only the quantization error introduced by the TDCs remains. With Eq. (7), it can be shown that the lifetime resolvability is greatly improved. Differentiating Eq. (6), the corresponding precision can be easily obtained by

$$\frac{\sigma\tau_{CMM,Corr}}{\tau} = \frac{\sigma\tau_{CMM}}{\tau}\left(\frac{d\tau_{CMM}}{d\tau}\right)$$

$$= \frac{h}{\tau\sqrt{N_c}}\frac{\sqrt{P(x)}(1-x^M)}{(1-x)\left[(1-x^M)^2 - \frac{M^2h^2}{\tau^2}x^M\right]}. \quad (9)$$

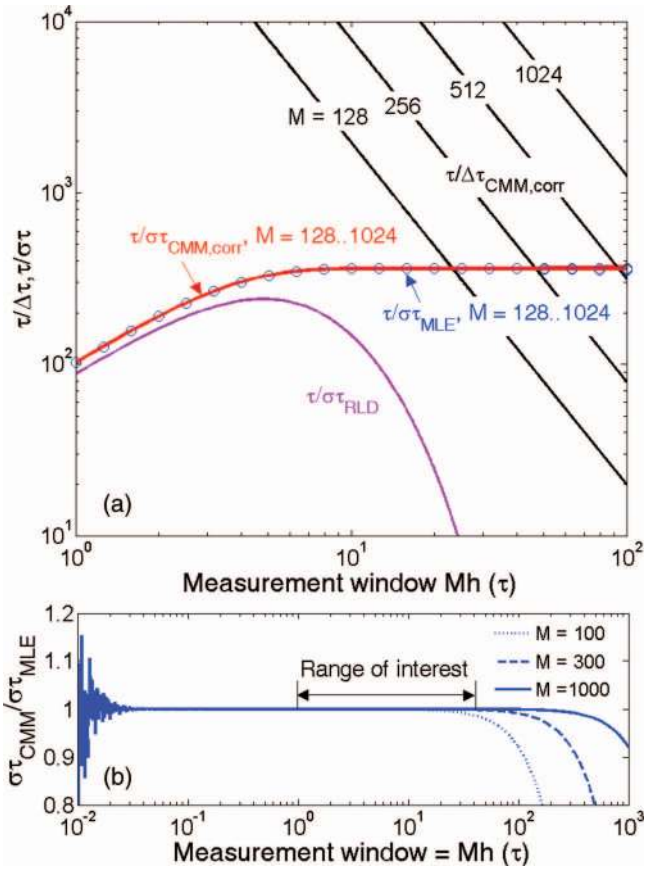

Fig. 2 (a) Inverse precision and accuracy curves for the corrected CMM, MLE, and 2-gate RLD with $N_c = 2^{17}$ (Measurement window: $Mh = 2w_g$) and (b) the ratio of the standard variation obtained by the corrected CMM to that obtained by the MLE for different values of M.

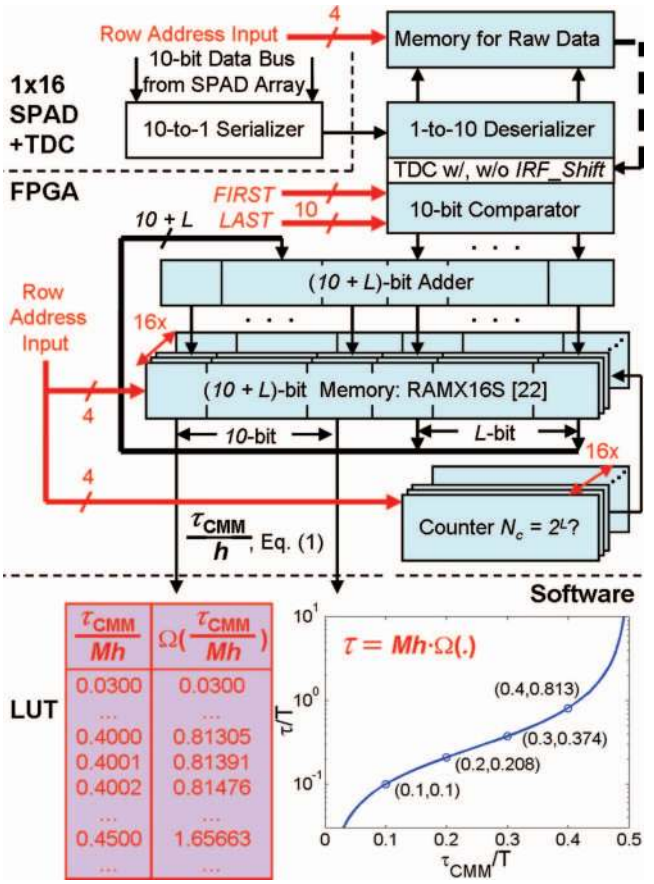

Fig. 3 On-FPGA CMM implementation for a column (1×16) of SPADs.

For MLE,[15] the precision is

$$\frac{\sigma\tau_{MLE}}{\tau} = \frac{\tau}{h\sqrt{N_c}}\frac{(1-x)(1-x^M)}{\sqrt{P(x)}}. \tag{10}$$

Figure 2(a) shows the inverse accuracy and precision curves of Eqs. (8), (9), and (10) for $M = 128$, 256, 512, 1024, and $N_c = 2^{17}$. The precision curves for the corrected CMM and MLE are almost the same in $1 < T/\tau < 100$. Compared with uncorrected CMM in Ref. 14, the accuracy of the corrected CMM is greatly improved, and its precision performance is comparable to and better than RLD in $1 < T/\tau < 4$ and $T/\tau > 4$, respectively. The precision curves of the corrected CMM are in good agreement with MLE ones for different values of M. Smaller Ms only result in higher quantization errors. Figure 2(b) shows the ratio of the precision obtained by Eq. (9) to that obtained by Eq. (10) for different values of M, and it shows that Eq. (9) is equivalent to Eq. (10) in the lifetime range of interest $1 < T/\tau < 100$. For $M = 100$, the ratio deviates from 1.0 as the estimator contains a significant bias for $T/\tau > 40$. It is not sensible to operate CMM beyond this range, since system nonidealities such as the full width at half maximum (FWHM) of the instrument response function (IRF) should be considered and the system is not designed for detecting a fluorescence lifetime much larger than 100 ns.

2.3 *On-FPGA Implementation of Center of Mass Method for Low Dark Count Single-photon Avalanche Diode Arrays*

We rewrite Eq. (1) as

$$\frac{\tau_{CMM}}{h} = \frac{\sum_{i=1}^{N_c}\bar{D}_i}{N_c} + \frac{1}{2}, \tag{11}$$

where $\bar{D}_i$ is the 10-bit TDC output of the ith captured photon. The lifetime can be updated when the counter storing N_c reaches a value of

$$N_c = 2^L, L \text{ is an integer}, \tag{12}$$

or when the frame counter reaches a certain number set by a user-defined value. The FPGA shown in Fig. 1(b) takes 2×32 parallel signals from two 32×16 SPAD arrays (with fast and slow TDC test sub-arrays). Figure 1(c) shows half the SPAD array (32×16) connected to on-FPGA CMM processing. Figure 3 shows the CMM implementation for one column of SPADs (1×16) on the Spartan-III FPGA. The rationale of implementing CMM on-FPGA is to evaluate the possibility of implementing CMM on-chip. On-chip CMM can act as a data compressor allowing a high resolution SPAD imager to operate at a higher frame rate (instead of 1 MHz in Ref. 21) without challenging the readout bandwidth of output pads. The prototype is aimed to provide both real-time FLIM and raw arrival time data

for scientific research. Unlike the one used in Ref. 14 for single-detector sensing systems, the new FPGA processor contains a 4-bit row address signal synchronized to the row number of each half of the SPAD array. The row address signal first points to the on-FPGA memory RAM16×1S (Ref. 22) (width = 10 + L) where a previous sum is stored. The detected TDC value for the corresponding pixel is passed to the 10-bit comparator for comparison with the user-defined parameters, *FIRST* and *LAST*, which define the measurement window. If the TDC value is within the window, the content is loaded and summed with the new TDC data, and a new summing result from the adder output will then update the content in the memory. The camera contains a memory controller for recording the raw data, which can provide information such as, locations of high-DCR pixels (DCR > 500 Hz, denoted as noisy pixels hereafter for they exhibit higher dark count noise), IRFs of pixels, and TDC uniformity, etc. When the condition in Eq. (12) is met or a certain frame number is reached, the lifetime is updated. The corrected lifetime can be obtained by

$$\tau = \Omega\left(\frac{\tau_{CMM}}{T}\right)\cdot T = \Omega\left[\frac{1}{M}\left(\frac{\sum_{i=1}^{N_c}\bar{D}_i}{N_c}+\frac{1}{2}\right)\right]\cdot Mh, \tag{13}$$

where $\Omega(*)$ is the LUT that maps a normalized τ_{CMM} to a normalized τ (see Fig. 3). The parameter $M = FIRST - LAST + 1$, and it is straightforward for the software to calculate τ by Eq. (13) with the already known M and h. The memory required to store the photon count N_c for each pixel works similarly but with a size of 16L-bits. The total memory size for a column of SPADs (1×16) is (160 + 32L)-bits. Therefore, for a whole array of SPADs (32×32), the memory usage is 2×32 × (160 + 32L) = (10 + 20L) k-bits. From Fig. 2(b) and Eqs. (9) and (10), we have established an algorithm virtually equivalent to MLE in the lifetime range of interest with the advantage that CMM has a much simpler 1-D LUT only depending on T/τ rather than both M and T/τ [Ref. 15, Eq. (4)]. When the camera is used for $T > 7\tau$, Eq. (13) can be bypassed.

3 Experimental Results

3.1 *Corrected CMM Fluorescence Lifetime Imaging Analysis on DNA Microarrays*

To evaluate the suitability of CMM for fluorescence lifetime imaging applications in realistic experimental conditions we first present post-processed (software-based) CMM of TCSPC data collected from DNA microarrays.[27] DNA microarrays consisting of 16 spots where incubated with (a) hepatitis C virus (HCV) probe, (b) human cytomegalovirus (HCMV) probe, and (c) a 1:1 molar ratio of these two probes. The arrays were hybridized with a 10-nM solution of fluorescently labeled complementary targets with a distinctly different excited state lifetime: HCV targets were labeled with Alexa Fluor 430 and HCMV with quantum dot (Qdot525) with lifetimes of approximately 4.2 and 22 ns,[28] respectively. The labeled microspot arrays were imaged using total internal reflection fluorescence (TIRF) illumination and TCSPC histograms were recorded using 32×16 SPAD + TDC array with 55 ns range. Details of the experimental procedures are given elsewhere.[27]

Figure 4(a) shows a fluorescence histogram collected by a pixel, a tail-fitted decay using the proposed CMM, and the residual plot for the Qdot525 labeled HCMV probes. Figure 4(b) shows the estimated lifetime and precision curves versus the measurement window (M = 200 to 800; $0.5 < T/\tau < 2$) for different algorithms. The uncorrected CMM, Eq. (1), suffers a significant bias even with the maximum measurement window the TDC can provide. For M = 200, the uncorrected CMM obtains a lifetime of 5 ns, which is far from the reality! The results obtained by the corrected CMM, Eqs. (7) or (13) converge to those obtained by the MLE as M increases and are slightly better than those by RLD, which is in good agreement with Fig. 2(a). The corrected CMM can extend the resolvability range down to $Mh = 0.5\tau$, but the measurement window is usually chosen as $Mh = 2$ to 5τ for better precision. Figure 4(c) shows the photon count (intensity) and lifetime images for the 10 nM Qdot525 labeled microspots using M = 500.

The analysis can be repeated for Alexa labeled HCV microspots. Figure 5(a) shows a fluorescence histogram collected by a pixel, a tail-fitted decay using the proposed CMM, and the residual plot. Figure 5(b) shows the estimated lifetime and precision versus the measurement window (M = 100 to 800; $1 < T/\tau < 10$) for different algorithms. As the signal levels are lower, the background plays a more significant role and contributes to the loss of precision for a larger M. There exists a trade-off between samples with different lifetimes. Nevertheless, the algorithm provides reliable lifetime estimates when simultaneously imaging differently labeled spots as shown in Fig. 6(a) using M = 500. The lifetime map and the corresponding lifetime histogram shown in Fig. 6(b) are in good agreement with the results reported in Ref. 27, Fig. 3(d). Note that for the two mixed (both labels present) spots the delay is clearly multi-exponential. CMM returns an estimate of the average lifetime, losing information about the decay dynamics but providing enough contrast to clearly distinguish the three types of microspots. From Eq. (1), for a double-exponential decay $f(t) = A_1\exp(-t/\tau_1) + A_2\exp(-t/\tau_2)$, the calculated lifetime using the uncorrected CMM is

$$\begin{aligned}\tau_{CMM} &\cong \frac{\int_0^T tf(t)dt}{\int_0^T f(t)dt}\\ &= \frac{A_1\tau_1^2 e^{-t/\tau_1}\left(-\frac{t}{\tau_1}-1\right)\Big|_0^T + A_2\tau_2^2 e^{-t/\tau_2}\left(-\frac{t}{\tau_2}-1\right)\Big|_0^T}{-A_1\tau_1 e^{-t/\tau_1}\big|_0^T - A_2\tau_2 e^{-t/\tau_2}\big|_0^T}.\\ &= \frac{A_1\tau_1^2 - A_1\tau_1^2 e^{-T/\tau_1}\left(\frac{T}{\tau_1}+1\right) + A_2\tau_2^2 - A_2\tau_2^2 e^{-T/\tau_2}\left(\frac{T}{\tau_2}+1\right)}{A_1\tau_1 - A_1\tau_1 e^{-T/\tau_1} + A_2\tau_2 - A_2\tau_2 e^{-T/\tau_2}},\end{aligned} \tag{14}$$

and the proposed system will provide a calculated lifetime $\tau = \Omega(\tau_{CMM}/T)\cdot T$ from Eq. (13). For A_1:A_2 = 1:1, 1:2, 1:3, 2:1, 3:1 with the measurement window above, the lifetimes are 14.0, 17.1, 18.5, 11.3, and 9.8 ns, respectively.

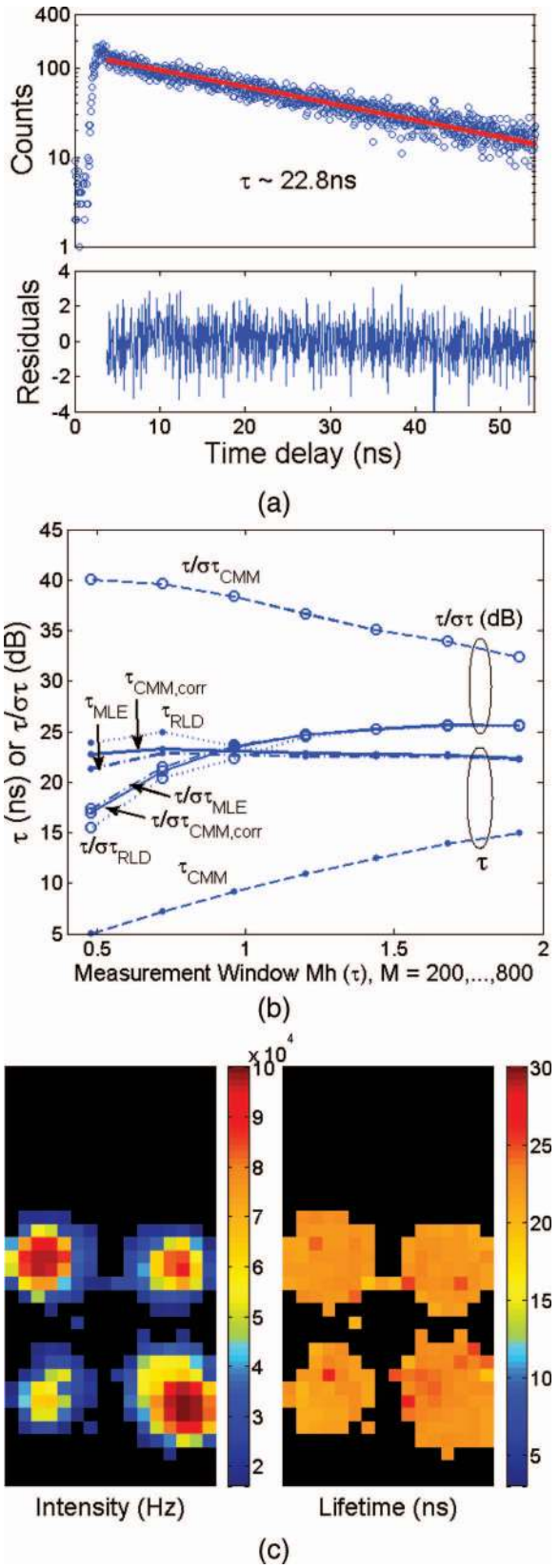

Fig. 4 (a) Fluorescence histogram and residual curves obtained by the proposed CMM, (b) lifetime and precision curves for different algorithms, and (c) intensity and lifetime images of quantum-dot labeled DNA microarray using $M = 500$.

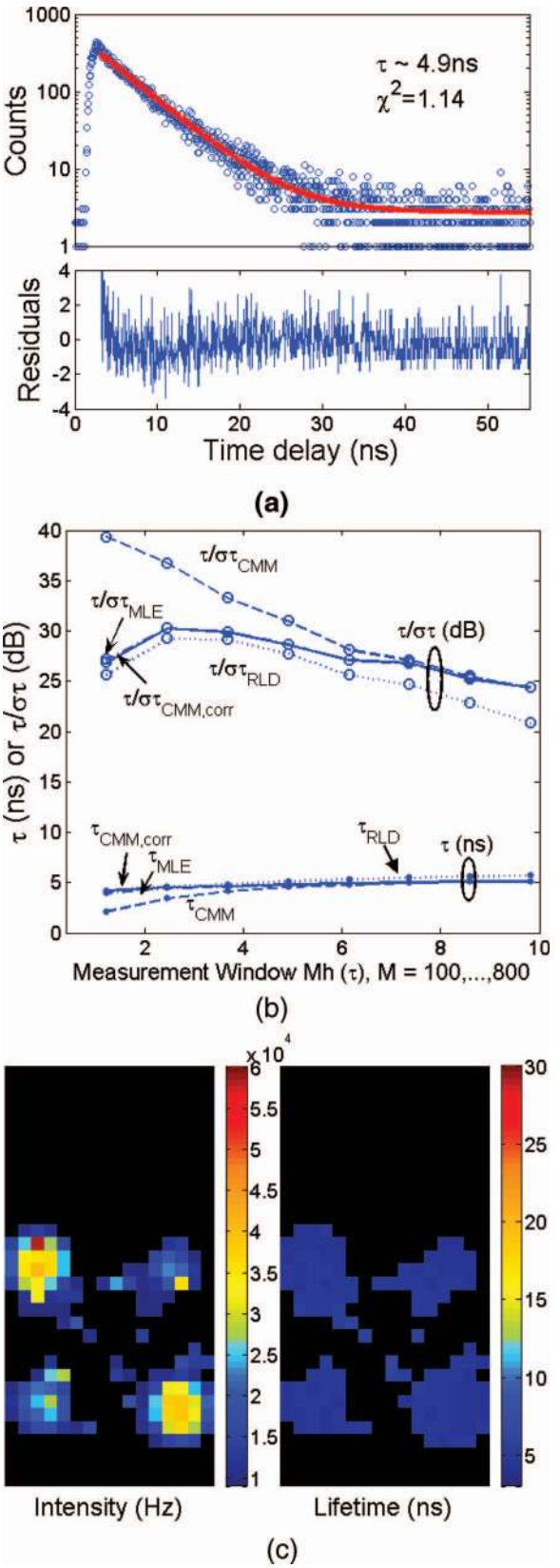

Fig. 5 (a) Fluorescence histogram and residual curves for Alexa obtained by the proposed CMM, (b) lifetime and precision curves for different algorithms, and (c) intensity and lifetime images of Alexa labeled DNA microarray with $M = 500$.

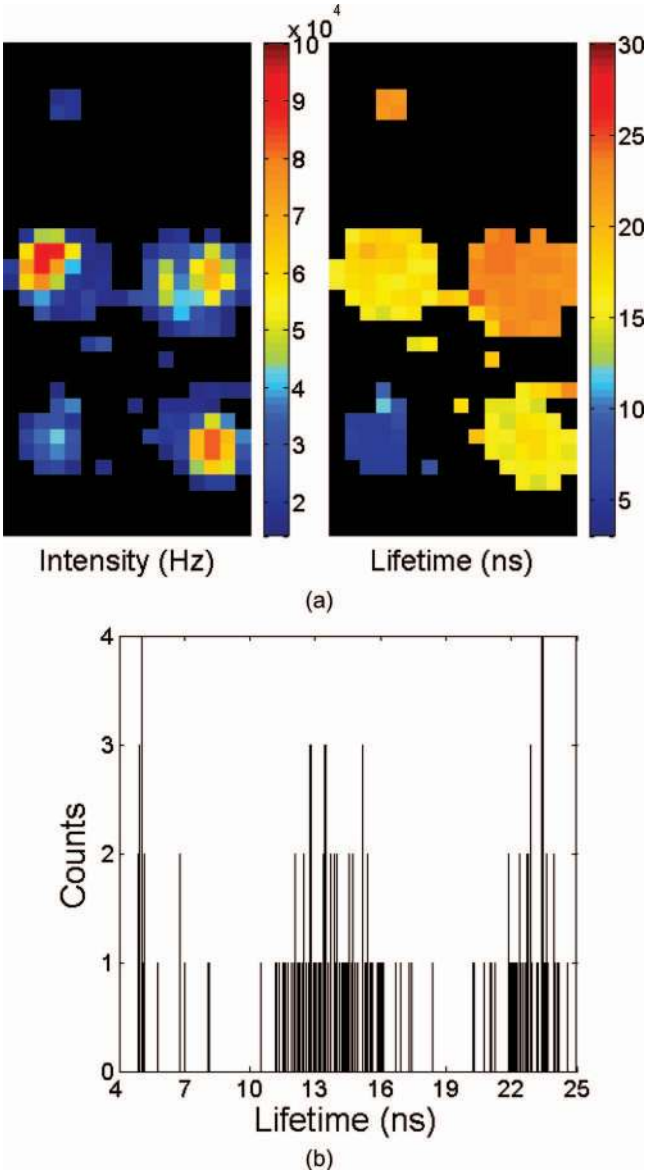

Fig. 6 (a) Intensity and lifetime images of Qdot525 labeled, Alexa labeled, and 1:1 molar ratio of Qdot525/Alexa labeled DNA microarray and (b) lifetime histogram.

3.2 *Fluorescence Lifetime Estimation Based on Low Number of Photon Events*

3.2.1 *Fluorescence lifetime imaging on Rhodamine B*

To achieve high-speed FLIM imaging, it is desirable to study the error performance when using a low number of photon events. For experimental demonstration of the CMM hardware lifetime calculation algorithm, a standard fluorescence lifetime wide-field imaging system was set up on a Nikon TE2000U inverted microscope. The excitation source was a PicoQuant pulsed diode laser with a wavelength of 470 nm coupled through the epi-fluorescence port of the microscope using a Nikon B-2A filter cube. The laser pulse rate is 20 MHz and the maximum power reaching the back focal plane of the objective is about 90 μW. The sample was imaged onto the 32×32 SPAD camera directly attached to one of the camera ports using a 20× objective (Nikon Plan Apo, 20×, NA 0.45). The TDC resolution is set to be 78 ps with the on-chip phase-locked loop enabled.[21] The IRF was measured by replacing the sample with a mirror and removing the emission filter so that the excitation light was found to have a FWHM of 0.6 ns.

First, a uniform sample of an aqueous solution of Rhodamine B was imaged, which makes it possible to assess the influence of inter-pixel variations. Each pixel has its own physically distinct SPAD and TDC leading to slightly different characteristics for each pixel. About 13% of the SPADs have a DCR in excess of 500 Hz and the peak position of the IRF has a standard deviation of about five bins due to variations in the time offset. We used the raw data stored in the memory to predict the error performance of the on-FPGA CMM. A measurement window of $100h$ ($M = 100$; $Mh/\tau \sim 4.1$) was chosen to calculate lifetimes. Two global window parameters *FIRST* and *LAST* ($= FIRST + M - 1$) can be set by users even without knowing the precise peak position of each IRF. For more accurate imaging, IRFs of all the pixels can be recorded, and the shift of their peak positions $\Delta FIRST$ relative to *FIRST*, can be added to the detected TDC value for each pixel such that the peaks for all histograms would align for the best photon efficiency. For fast demonstration, we only implemented the blue blocks of Fig. 3 on FPGA with a global *FIRST* set to all pixels (denoted as the global scheme hereafter). Figure 7(a) shows lifetime images obtained by the corrected CMM, for an average $N_c = 335$, 677, 1376, and 2774, respectively, with *FIRST* set for each pixel to the peak of its own histogram (denoted as the local scheme hereafter), but without the noisy pixels [~13% of pixels with DCR > 500 Hz (Ref. 21)] removed. The pattern of noisy pixels can be easily spotted, and it can be located during the characterization of the imager. It is desirable to exclude these noisy pixels to solely reveal the error performance of the algorithms. We applied simple median filtering only on the noisy pixels, and the lifetime images are shown as Fig. 7(b). Figure 7(c) shows lifetime images for an average $N_c = 281$, 562, 1123, and 2244, respectively, using the global scheme, which will be similar to the images generated from the on-FPGA CMM. Figure 7(d) shows lifetime versus N_c scattergrams with the noisy pixels excluded. From Eq. (9), the precision for the corrected CMM is about $3\log_2(N_c) - 1.5$ (dB) at $Mh/\tau \sim 4.1$ [$F \equiv \sqrt{N_c} \cdot \sigma\tau/\tau = 1.2$ (Ref. 29)]. Figures 7(e) and 7(f) show the precision curves versus N_c with the local and global schemes, respectively. The measurement window for RLD was chosen at its optimum condition for a fair comparison. The global scheme contributes to 1 to 2 dB of loss in precision and a bias of 0.03 ns due to some pixels having their peaks away from *FIRST*, but we can expect the loss will be smaller for resolving samples with larger lifetimes. The error performance of the corrected CMM is similar to that of MLE. With the global scheme, the proposed CMM can extract lifetimes with an SNR of 22 dB with only 281 counts ($F \sim 1.3$). The ideal curve is based on the MLE,[15] but without considering nonidealities of the system, such as jitter, uniformity, etc. The deviation from the ideal curve (note the F value is not 1.0, since we use a measurement window of 4.1τ where the optimum $F = 1.2$) comes from nonidealities such as jitter of the IRF, nonuniformity of the TDC resolution, and background, etc. Nevertheless, it provides reliable lifetime estimates and is enough for high-speed FLIM.

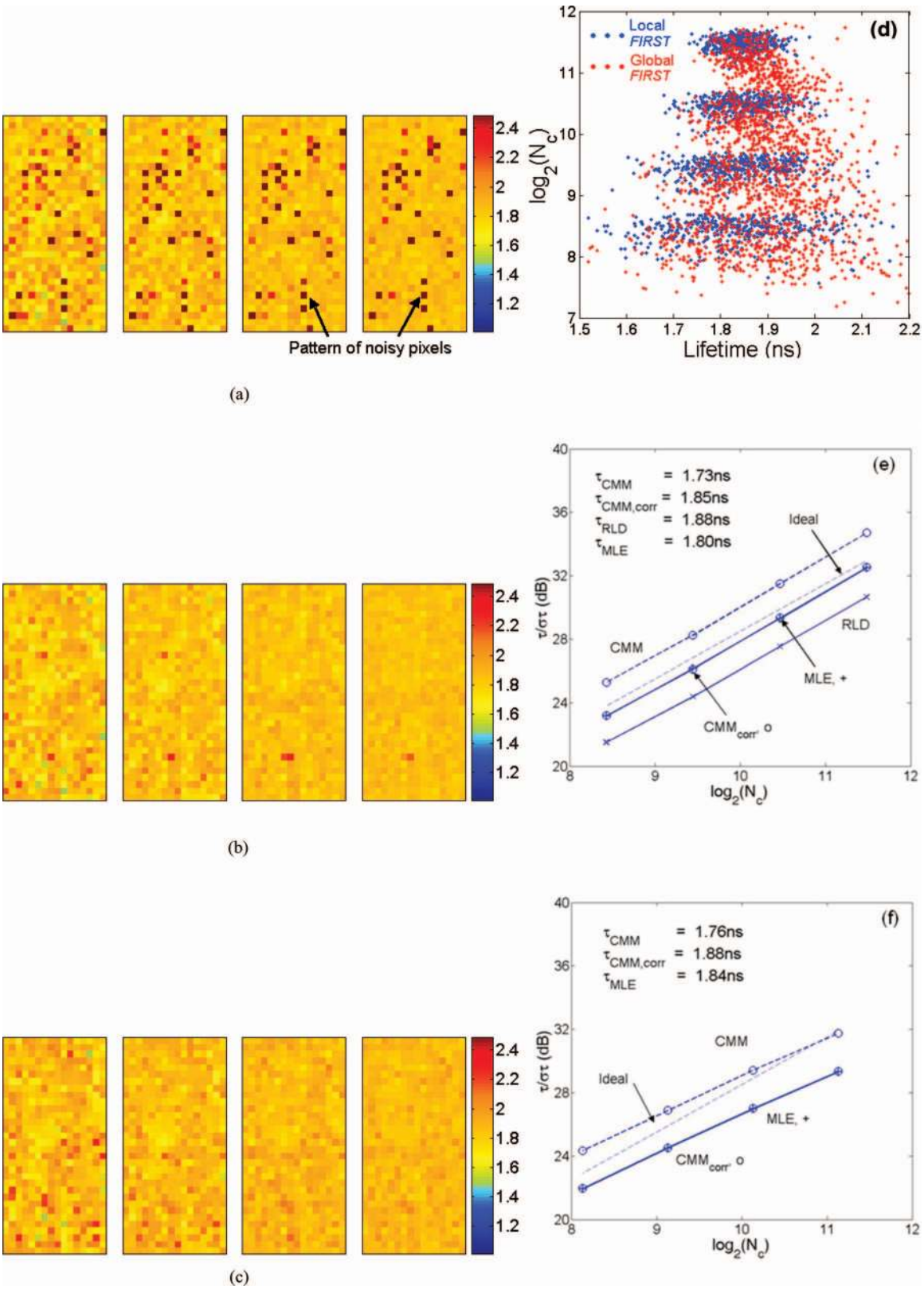

Fig. 7 (a) and (b) Lifetime images for different N_c with local *FIRST* scheme without and with noisy pixels filtered respectively, (c) lifetime images for different N_c with a global *FIRST*, (d) lifetime versus photon count scattergrams with noisy pixels excluded, precision plots with (e) the local scheme and (f) a global *FIRST*.

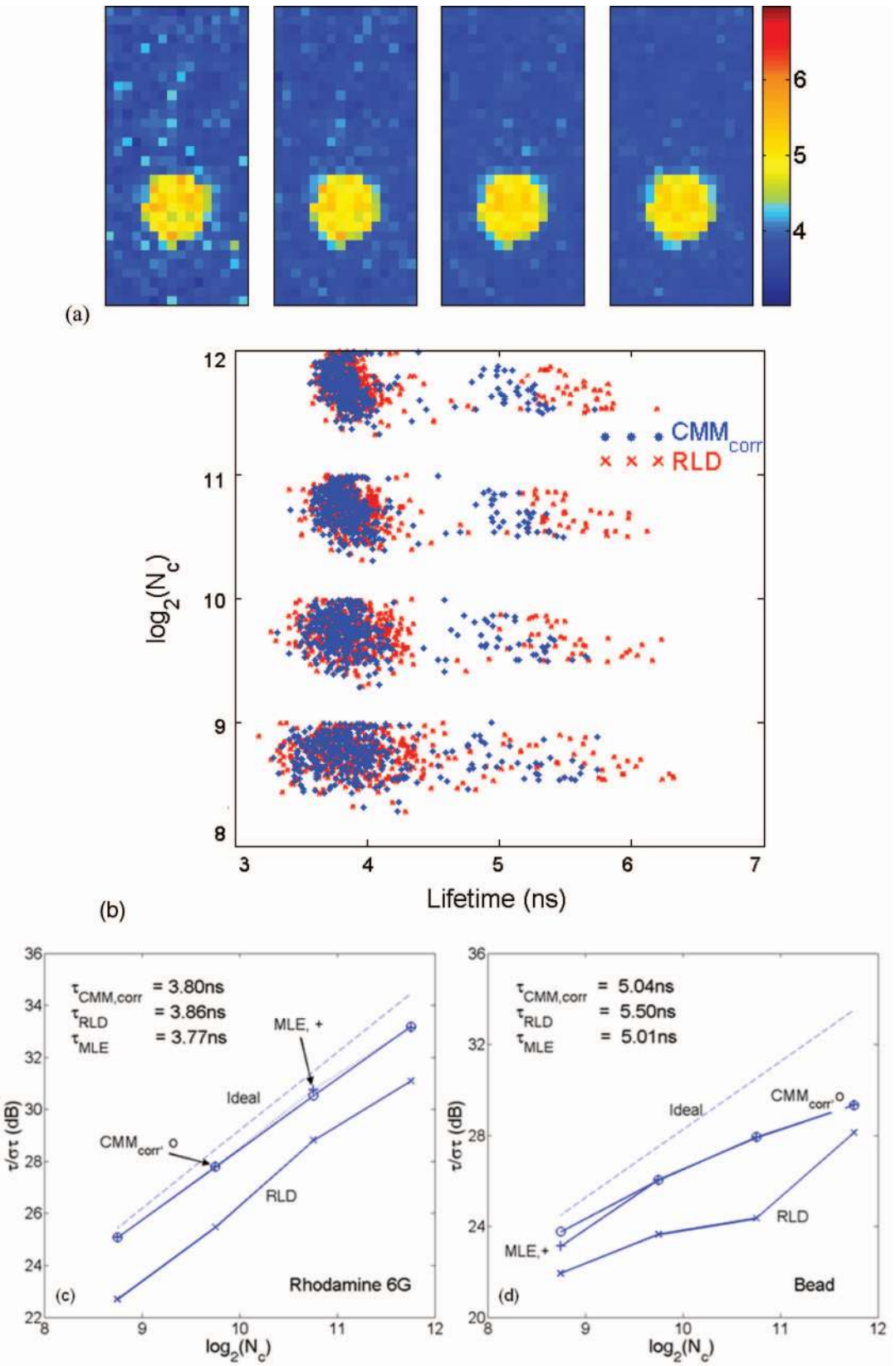

Fig. 8 (a) Lifetime images of fluorescent beads in Rhodamine 6G for different average photon counts, (b) lifetime versus photon count scattergrams with a global *FIRST*, (c) precision curves for Rhodamine 6G, and (d) precision curves for the bead in the measurement window ($M = 250$).

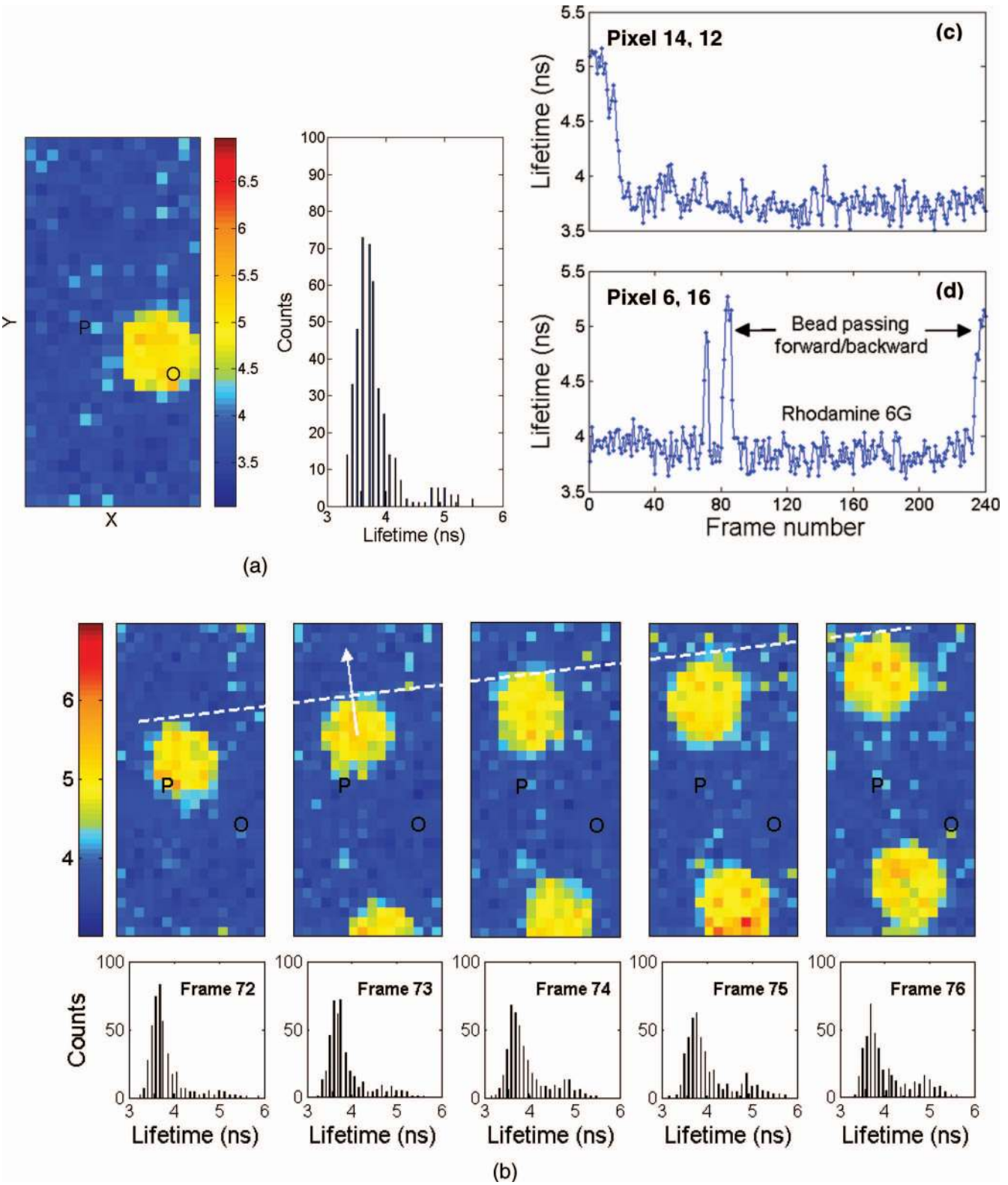

Fig. 9 (a) (Video 1) Fluorescence lifetime movie of fluorescent beads ($\tau = 5$ ns) in Rhodamine 6G ($\tau = 3.8$ ns), (b) 72nd to 76th frames of lifetime images and their corresponding lifetime histograms, respectively, and (c) and (d) estimated lifetimes of the pixels O (14, 12) and P (6, 16) versus the frame number, respectively. (Video 1, Quicktime, 5.7 MB) [URL: http://dx.doi.org/10.1117/1.3625288.1]

3.2.2 *Fluorescence lifetime imaging on fluorescent beads in Rhodamine 6G*

In order to study the error performance of the proposed on-FPGA CMM, we prepared a simple sample showing two distinct but similar lifetimes by suspending yellow-green fluorescent polystyrene beads of 15 μm diameter (Invitrogen, FluoSpheres, F8844) in an aqueous solution of Rhodamine 6G. The fluorescent solution was prepared very concentrated (1 mM) in order to achieve signal levels comparable to the bright beads.

But, before we demonstrate video-rate FLIM imaging on fluorescent beads in Rhodamine 6G, it is desirable to study the error performance of the proposed on-FPGA CMM on a static sample. By doing so, we can expect what we are going to see on the video. We choose $M = 250$ ($Mh \sim 5\tau$ for Rhodamine 6G and $Mh \sim 4\tau$ for the beads) and a global *FIRST* for the whole array. Figure 8(a) shows the lifetime images of a fluorescent bead in Rhodamine 6G for an average N_c of 430, 862, 1726, and 3454, respectively. Figure 8(b) shows the scattergram of the lifetimes versus the photon counts for the RLD (gate width $w_g = 2 \sim 2.5\tau$) and corrected CMM. The measurement window for RLD was chosen at its optimum condition for a fair comparison. Figures 8(c) and 8(d) show the precision plots for Rhodamine 6G and beads, respectively. The error performance of the corrected CMM is similar to that of MLE. The CMM performs better than RLD for resolving Rhodamine 6G with a margin of 2 dB. The number of pixels covering the bead is small, and that is why we have a higher deviation. The lifetimes can be estimated from the lifetime histograms and they are 3.8 ns for Rhodamine 6G and 5.0 ns for the bead, both in good agreement with the data provided by the manufacturers.

3.3 *Video-Rate Fluorescence Lifetime Imaging on Fluorescent Beads in Rhodamine 6G*

To demonstrate video-rate performance, the sample stage holding a sample of fluorescent beads in Rhodamine 6G was translated, simulating flow of tracer particles in a microfluidic cell sorter system. From the discussion in Sec. 3.2, we choose $M = 250$, a global *FIRST* for the whole array, and $L = 10$ ($N_c = 1024$).

Figure 9(a) (Video 1) shows the first frame of the lifetime image and the corresponding lifetime histogram of the video, 240 frames in total. The lifetime images are generated at a frame speed of 50 fps (lifetimes updated at a rate higher than 100 Hz), but the video is played at a $\times 0.6$ speed, 30 fps. We applied median filtering to remove the noisy pixels on FLIM images, and the noisy pixels were also excluded from the lifetime histogram solely to reveal the performance of the proposed algorithm. Figure 9(b) shows the 72nd to 76th frames of lifetime images and their corresponding lifetime histograms, respectively, as a new bead goes into the field of view. The size of the bead is 15 μm. The speed of the translating stage reaches up to 200 μm/s. The 76th frame contains two beads, and the lifetimes of the Rhodamine 6G and the beads with noisy pixels removed are 3.8 ns ($\sigma\tau \sim 0.19$ ns) and 5.0 ns ($\sigma\tau \sim 0.25$ ns), respectively. Their precisions are both around 26 dB close to the estimation on the precision plots shown in Figs. 8(c) and 8(d). Figures 9(c) and 9(d) show the estimated lifetimes of the pixels (14, 12) marked as "O" and (6, 16) marked as "P" versus the frame number, respectively. During the video recording, the sample stage was initially static for 15 frames and it started to move. The top speed can be observed from the 72nd to 76th frames. After that, it was slowed down and then moved backward from the 160th frame. Throughout the video, only one bead passed the pixel (14, 12), whereas two beads passed the pixel (6, 16) with the first bead marginally passing it once and the second one passing it forward and backward with different speeds.

4 Conclusion

A newly proposed FPGA algorithm for single-detector fluorescence lifetime sensing systems, CMM, has been successfully improved and employed for high-speed FLIM imaging applications. It can be viewed as a hardware implementation algorithm for the commonly used MLE method, as it has very similar performance but only needs a simple 1D LUT rather than a 2D LUT that depends on both M and h. To demonstrate its performance, a wide-field microscope was adapted to accommodate a 0.13 μm CMOS 32×32 SPAD + TDC array to test different fluorescent samples. Video-rate FLIM imaging with a frame rate over 50 fps can be achieved and has been demonstrated on fluorescent beads in Rhodamine 6G. The calculated lifetimes are in good agreement with those obtained by commercially available software. To enhance the lifetime resolving range, the previously proposed algorithm has been modified by introducing a LUT on software and demonstrated on real data. We can expect our FLIM camera prototype with future improvements on firmware/software and with the mounted micro-lens array to improve sensitivity[30] to provide new applications for cellular imaging, such as proteomics, DNA microarray scanning, flow engineering, protein-DNA interactions,[31] and tissue imaging.[32]

Acknowledgments

The CMM hardware implementation and data analysis have been supported by the European Commission within the 7th Framework Programme, Health Research METOXIA project (HEALTH-F2–2009-222741, www.metoxia.uio.no). Tyndall is sponsored by an EPSRC Studentship. The CMOS SPAD chip has been supported by the European Commission within the 6th Framework Programme of the Information Science Technologies, Future Emerging Technologies Open MEGAFRAME project (Contract No. 029217–2, www.megaframe.eu). The authors would like to thank Dr. Wei Wang for his comments on this work.

References

1. S. Cova, M. Ghioni, A. Lacaita, C. Samori, and F. Zappa, "Avalanche photodiodes and quenching circuits for single-photon detection," *Appl. Opt.* **35**, 1956–1976 (1996).
2. S. Cova, M. Ghioni, A. Lotito, I. Rech, and F. Zappa, "Evolution and prospects for single-photon avalanche diodes and quenching circuits," *J. Mod. Opt.* **51**, 1267–1288 (2004).
3. L.-Q. Li and L. M. Davis, "Single photon avalanche diode for single molecule detection," *Rev. Sci. Instrum.* **64**, 1524–1529 (1993).
4. H. Yang, G. Luo, P. Karnchanaphanurach, T.-M. Louie, I. Rech, S. Cova, L. Xun, and X. S. Xie, "Protein conformational dynamics probed by single-molecule electron transfer," *Science* **10**, 262–266 (2003).
5. C. Niclass, A. Rochas, P. A. Besse, and E. Charbon, "Design and characterization of a CMOS 3-D image sensor based on single photon avalanche diodes," *IEEE J. Solid-State Circuits* **40**, 1847–1853 (2005).

6. D. Stoppa, D. Mosconi, L. Pancheri, and L. Gonzo, "Single-photon avalanche diode CMOS sensor for time-resolved fluorescence measurements," *IEEE Sens. J.* **9**, 1084–1090 (2009).
7. D. E. Schwartz, P. Gong, and K. L. Shepard, "Time-resolved Förster-resonance-energy-transfer DNA assay on an active CMOS microarray," *Biosens. Bioelectron.* **24**, 383–390 (2008).
8. B. R. Bae, K. J.-B. Yang, J. McKendry, Z. Gong, D. Renshaw, J. M. Girkin, E. Gu, M. D. Dawson, and R. K. Henderson, "A vertically integrated CMOS microsystem for time-resolved fluorescence analysis," *IEEE Trans. Biomed. Circ. Syst.* **4**, 437–444 (2010).
9. M. Gersbach, J. Richardson, E. Mazaleyrat, S. Hardillier, C. Niclass, R. Henderson, L. Grant, and E. Charbon, "A low-noise single-photon detector implemented in a 130 nm CMOS imaging process," *Solid-State Electron.* **53**, 803–808 (2009).
10. J. A. Richardson, L. A. Grant, and R. K. Henderson, "Low dark count single-photon avalanche diode structure compatible with standard nanometer scale CMOS technology," *IEEE Photon. Technol. Lett.* **21**, 1020–1022 (2009).
11. R. K. Henderson, E. A. G. Webster, R. Walker, J. A. Richardson, and L. A. Grant, "A 3×3, 5 mm pitch, 3-transistor single photon avalanche diode array with integrated 11 V bias generation in 90 nm CMOS technology," in *Proc. 2010 IEEE Int. Electron Devices Meeting (IEDM)*, pp. 14.2, Dec. 6–8, San Francisco, CA (2010).
12. E. A. G. Webster, J. A. Richardson, L. A. Grant, D. Renshaw, and R. K. Henderson, "An infra-red sensitive, low noise, single-photon avalanche diode in 90 nm CMOS," *International Image Sensor Workshop (IISW)*, Hokkaido, Japan, 8–11 June 2011.
13. R. A. Colyer, G. Scalia, I. Rech, A. Gulinatti, M. Ghioni, S. Cove, S. Weiss, and X. Michalet, "High-throughput FCS using an LCOS spatial light modulator and an 8×1 SPAD array," *Biomed. Opt. Express* **1**, 1408–1430 (2010).
14. D.-U. Li, B. Rae, R. Andrews, J. Arlt, and R. Henderson, "Hardware implementation algorithm and error analysis of high-speed fluorescence lifetime sensing systems using center-of-mass method," *J. Biomed. Opt.* **15**, 017006 (2010).
15. P. Hall and B. Selinger, "Better estimates of exponential decay parameters," *J. Phys. Chem.* **85**, 2941–2946 (1981).
16. D. S. Elson, I. Munro, J. Requejo-Isidro, J. McGinty, C. Dunsby, N. Galletly, G. W. Stamp, M. A. A. Neil, M. J. Lever, P. A. Kellett, A. Dymoke-Bradshaw, J. Hares, and P. M. W. French, "Real-time time-domain fluorescence lifetime imaging including single-shot acquisition with a segmented optical image intensifier," *New J. Phys.* **6**, 1–13 (2004).
17. M. Elangovan, R. N. Day, and A. Periasamy, "Nanosecond fluorescence resonance energy transfer-fluorescence lifetime imaging microscopy to localize the protein interactions in a single living cell," *J. Microsc.* **205**, 3–14 (2002).
18. G. I. Redford and R. M. Clegg, "Real-time fluorescence lifetime imaging and FRET using fast gated intensifiers," in *Molecular Imaging: FRET Microscopy and Spectroscopy*, A. Periasamy and R. N. Day, Eds., pp. 193–226, Oxford University, New York (2005).
19. A. Leray, F. B. Riquet, E. Richard, C. Spriet, D. Trinel, and L. Héliot, "Optimized protocol of a frequency domain fluorescence lifetime imaging microscope for FRET measurements," *Microsc. Res. Tech.* **72**, 371–379 (2009).
20. A. C. Mitchell, J. E. Wall, J. G. Murray, and C. G. Morgan, "Direct modulation of the effective sensitivity of a CCD detector: a new approach to time-resolved fluorescence imaging," *J. Microsc.* **206**, 225–232 (2002).
21. J. Richardson, R. Walker, L. Grant, D. Stoppa, F. Borghetti, E. Charbon, M. Gersbach, and R. Henderson, "A 32×32 50 ps resolution 10 bit time to digital converter array in 130 nm CMOS for time correlated imaging," in *Proc. IEEE Custom Integrated Circuits Conf. (CICC)*, pp. 77–80, Sept. 13–16, San Jose, CA (2009).
22. *Spartan-III FPGA Family Data Sheet: Complete Data Sheet*, Datasheet DS099 (v2.5), Xilinx, Inc., San Jose, CA (2009).
23. R. M. Ballew and J. N. Demas, "An error analysis of the rapid lifetime determination method for the evaluation of single exponential decays," *Anal. Chem.* **61**, 30–33 (1989).
24. A. V. Agronskaia, L. Tertoolen, and H. C. Gerritsen, "Fast fluorescence lifetime imaging of calcium in living cells," *J. Biomed. Opt.* **9**, 1230–1237 (2004).
25. D.-U. Li, B. Rae, E. Bonnist, D. Renshaw, and R. Henderson, "On-chip fluorescence lifetime extraction using synchronous gating scheme: theoretical error analysis and practical implementation," in *Proc. Int. Conf. Bio-inspired Systems and Signal processing*, Funchal, Portugal, pp. 171–176 (2008), INSTICC, Lisbon, Portugal.
26. C. Moore, S. P. Chan, J. N. Demas, and B. A. Degraff, "Comparison of methods for rapid evaluation of lifetime of exponential decays," *Appl. Spectrosc.* **58**, 603–607 (2004).
27. G. Giraud, H. Schulze, D.-U. Li, T. T. Bachmann, J. Crain, D. Tyndall, J. Richardson, R. Walker, D. Stoppa, E. Charbon, R. Henderson, and J. Arlt, "Fluorescence lifetime biosensing with DNA microarrays and a CMOS-SPAD imager," *Biomed. Opt. Express* **1**, 1302–1308 (2010).
28. G. Giraud, H. Schulze, T. T. Bachmann, C. J. Campbell, A. R. Mount, P. Ghazal, M. R. Khondoker, A. J. Ross, S. W. J. Ember, I. Ciani, C. Tlili, A. J. Walton, J. G. Terry, and J. Crain, "Fluorescence lifetime imaging of quantum dot labeled DNA microarrays," *Int. J. Mol. Sci.* **10**, 1930–1941 (2009).
29. A. Draaijer, R. Sanders, and H. C. Gerritsen, "Fluorescence lifetime imaging, a new tool in confocal microscopy," in *Handbook of Biological Confocal Microscopy*, J. Pawley, Ed., pp. 491–505, Plenum, New York (1995).
30. S. Donati, G. Martini, and M. Norgia, "Microconcentrators to recover fill-factor in image photodetectors with pixel on-board processing circuits," *Opt. Express* **15**, 18066–18075 (2007).
31. F. G. E. Cremazy, E. M. M. Manders, P. I. H. Bastiaens, G. Kramer, G. L. Hager, E. B. van Munster, P. J. Verschure, T. W. J. Gadella Jr., and R. van Driel, "Imaging in situ protein-DNA interactions in the cell nucleus using FRET-FLIM," *Exp. Cell Res.* **309**, 390–396 (2005).
32. D. Elson, R. Requejo-Isidro, I. Munro, F. Reavell, J. Siegel, K. Suhling, P. Tadrous, R. Benninger, P. Lanigan, J. McGinty, C. Talbot, B. Treanor, S. Webb, A. Sandison, A. Wallace, D. Davis, J. Lever, M. Neil, D. Phillips, G. Stamp, and P. French, "Time-domain fluorescence lifetime imaging applied to biological tissue," *Photochem. Photobiol. Sci.* **3**, 795–801 (2004).